Edge vortex interaction minimizes drag in shrimp swimming

Zhipeng Lou [1], Nils Tack [2], Monica M. Wilhelmus [2] and Chengyu Li [1,*]
[1] *Department of Mechanical and Aerospace Engineering, Case Western Reserve University, Cleveland, Ohio 44106, USA*
[2] *School of Engineering, Brown University, Providence, Rhode Island 02912, USA*

(Received 6 August 2024; accepted 20 March 2025; published 18 April 2025)

Shrimp swim by metachronal paddling with five pairs of appendages known as pleopods, which create and detach vortices at their tips and edges. The tip vortices produced by adjacent pleopods are thought to interact, potentially enhancing hydrodynamic performance. Although edge vortices have garnered less focus, their interactions may also contribute positively to propulsion. In this study, we created a three-dimensional, high-fidelity reconstruction of a forward steady-swimming marsh grass shrimp (*Palaemon vulgaris*), based on high-speed recordings. By solving the flow field using the reconstructed model in our in-house computational fluid dynamics solver, we conducted a series of parametric studies to investigate the effect of interappendage interaction. Our results show that the shrimp experiences a 20.46% increase in the cost of transport without interappendage interactions. During the recovery stroke, these interactions can reduce drag by 272.94% and power consumption by 137.30%. These propulsion improvements are primarily due to interactions between edge vortices from adjacent pleopods. During the recovery stroke, pleopods move closer together, allowing edge vortices to merge. This merger aligns the flow in front of the pleopods with their stroke direction, creating a strokeward flow that reduces pressure on the anterior surface of the pleopods and consequently decreases drag.

DOI: 10.1103/PhysRevFluids.10.043103

I. INTRODUCTION

Metachronal swimming is a common locomotory strategy using drag-based propulsion adopted by various aquatic organisms, such as shrimp [1–4], krill [5–7], ctenophores [8–11], and *Tomopteris* worms [12,13]. Each appendage of a metachronal swimmer performs a propulsive power stroke to generate thrust, followed by a recovery stroke to reposition for the next cycle, generating drag. To coordinate multiple appendages, these organisms rhythmically stroke their appendages in an array or a row with specific phase lags relative to adjacent ones, creating a metachronal wave along their body [14]. Most metachronal swimmers use antiplectic coordination, where the power stroke direction is opposite to the wave propagation direction [8,15,16]. This coordination is believed to be more efficient for fluid transport and locomotion [6,17–20]. In drag-based propulsion, the drag generated by the recovery stroke can slow down forward motion, causing periodic deceleration, especially during single appendage paddling or when multiple appendages paddle synchronously [20,21]. In contrast, during metachronal paddling, some appendages are performing power strokes while others are recovering. The thrust generated by the power-stroking appendages exceeds the drag from the recovering appendages, resulting in overall acceleration that is greater than zero. This leads to consistent propulsion, functioning similarly to a multicylinder piston engine [22].

*Contact author: cxl1692@case.edu

To further enhance propulsive performance, various animals have evolved modifications to metachronal motion, targeting either increased thrust during the power stroke or minimized drag during the recovery stroke. For instance, in marsh grass shrimp (*Palaemon vulgaris*) interappendage phase lag promotes the coalescence of up to three adjacent appendages during their recovery stroke to lower drag, thereby enhancing the net thrust [4]. Other arthropods, such as copepods, partially replace the metachronal motion with a synchronous motion during the recovery stroke which creates a greater clearance for a larger stroke amplitude [20,23–25]. This larger stroke amplitude facilitates higher peak acceleration during power strokes, enhancing thrust [3,25]. The synchronous recovery strokes of copepods also reduces drag by overlapping appendages closely [24]. Besides coordination of multiple appendages, many animals have evolved the ability to morph their appendages. For example, polychate worms [13] and marsh grass shrimp [4] have flexible appendages that bend asymmetrically and spread during the power stroke to increase thrust by expanding the surface area and collapse during the recovery stroke to reduce drag by minimizing the surface area. Similar mechanisms combining thrust enhancement and drag reduction are also observed in ctenophores [9], *Balanus* spp. cyprid [26,27], polychaetes [13] and remipedes [28]. The key to such enhancement mechanism is to maximize the difference between thrust generated during the power stroke and drag generated during the recovery stroke through area differences.

In addition to the above explicit propulsion enhancement, animals can implicitly improve the performance by the interaction of multiple appendages. During paddling, the appendages generate vortex structures in the near field, including tip vortices, the vortices that attach at the tips of appendages. They periodically form and later detach. After the detachment, the tip vortices may interact with other tip vortices, where such interactions are believed to be beneficial. For example, Particle Image Velocimetry experiments on mantis shrimp observed that tip vortices generated by the anteriormost pleopod during the power stroke can be strengthened by the posteriormost appendage, which potentially improves the swimming [1]. In contrast, in marsh grass shrimp, the tip vortex forming during the recovery stroke of the posteriormost appendage is observed to be transferred successively to the anterior pleopods rather than being shed in the free stream, thus inducing no wake during the pleopod recovery phase and reducing drag [4]. These effects of interaction may depend on the phase lag, root spacing, spatial asymmetry (i.e., bending), and Reynolds number [4,21,29]. Moreover, the interaction among tip vortices before their detachment becomes more pronounced during the recovery stroke due to the closer tips. For instance, during the recovery stroke, as appendages come close together, tip vortices generated by adjacent appendages form a shear layer that leads to a tip vortex weakening mechanism, reducing the drag force from the recovery stroke [22]. Such drag reduction during the recovery stroke can also reduce power consumption, which becomes an important design factor when power expenditure is a major concern.

Besides the interactions among tip vortices, interactions among other vortex structures may also positively impact metachronal propulsion. For instance, evidence suggests that when a flat plate encounters flow at a certain angle of attack, a vortex sheet forms over the plate. The edges of this sheet roll up due to flow separations, creating both tip and edge vortices [30,31]. Similarly, a paddling appendage generates both tip and edge vortices. During metachronal paddling, the closer spacing of appendages during the recovery stroke facilitates interactions not only among approaching tip vortices but also among edge vortices. Metachronal swimming animals may potentially leverage these interactions to enhance propulsion. However, only a few studies [32] have investigated whether edge vortex interactions influence the hydrodynamic performance of metachronal swimming.

Furthermore, existing literature on interappendage interactions primarily focuses on overall hydrodynamic performance. To study these interactions more quantitatively, it is beneficial to compare performance with and without interactions. This comparison can be achieved by evaluating the performance of one appendage paddling next to others versus an individual appendage paddling alone. While it is challenging to extract data from individual appendages of real animals, robotic models have the potential to acquire such data [4,6,21,30,33,34]. Additionally, numerical methods offer the convenience of extracting performance data for each individual appendage. Numerical

TABLE I. Morphological parameters of the shrimp. L_b, body length; W, total weight. The averaged values among five appendages are bolded.

Protopodite (mm)		Exopodite (mm)		Pleopod (mm)		Spacing (mm)		General	
l_{prot1}	1.67	l_{exop1}	2.68	l_{pleo1}	4.34	d_{1-2}	1.91	W (mN)	2.04
l_{prot2}	1.90	l_{exop2}	2.67	l_{pleo2}	4.57	d_{2-3}	1.67	L_b (mm)	27.96
l_{prot3}	1.79	l_{exop3}	2.67	l_{pleo3}	4.46	d_{3-4}	1.59		
l_{prot4}	1.63	l_{exop4}	2.57	l_{pleo4}	4.20	d_{4-5}	1.93		
l_{prot5}	1.03	l_{exop5}	2.75	l_{pleo5}	3.79				
$\bar{\boldsymbol{l}}_{\text{prot}}$	1.60	$\bar{\boldsymbol{l}}_{\text{exop}}$	2.67	$\bar{\boldsymbol{l}}_{\text{pleo}}$	4.27	$\bar{\boldsymbol{d}}$	1.77		

models are also easy and cost-efficient for modifying parameters of the appendage row, such as adjusting the total number of appendages and their spacing [22]. However, there is currently a lack of sufficient numerical studies demonstrating interappendage interactions, particularly regarding the beneficial interactions among edge vortices.

In this study, we performed experiments to record high-speed videos of a free-swimming shrimp (*P. vulgaris*), which we used to reconstruct a three-dimensional high-fidelity model. Using an in-house computational fluid dynamics (CFD) solver, we numerically solved the flow field for a steady swimming shrimp to reveal the effects of interappendage interactions, particularly vortex interactions, on hydrodynamic performance. This includes analyzing hydrodynamic forces, power, and overall cost of transport (COT). We conducted a series of comparisons between the free-swimming shrimp, which has five pairs of appendages, and modified models with only one pair of appendages. Our analysis aims to answer three key questions: (1) What are the effects of interappendage interactions on hydrodynamic forces and the COT, including drag reduction during the recovery stroke and overall efficiency improvement? (2) How do edge vortices interact? (3) If they interact, how much do these interactions contribute to the overall effects of interappendage interactions? These findings will provide a deeper understanding of the interappendage interaction mechanisms in metachronal swimming and inspire future designs of underwater robots equipped with multiple robotic appendages.

II. METHODOLOGY

A. Morphological parameter and high-speed recordings

1. Collection and housing

Marsh grass shrimp (*P. vulgaris*; $n = 13$; body length, BL $= 3.11 \pm 0.25$ cm) were collected in June 2022 from Narragansett Bay (Rocky Point State Park, Warwick, RI, USA) and housed at room temperature (21 °C) in a 38-l aquarium with salinity of 30‰. The capture and analyses were conducted in accordance with the laws of the State of Rhode Island.

2. Morphometric measurements

Body and appendage morphometrics (including the protopodite, endopodite, and exopodite of each leg; see Table I) were obtained digitally from scaled lateral images of shrimp specimens using IMAGEJ. Body length was measured as the distance from the tip of the rostrum to the tip of the telson in the forward swimming, as shown in Fig. 1(a). Note that because the first pleopod (P1) endopodite is sexually dimorphic, atrophied, and not involved in propulsion in *P. vulgaris*, the P1 endopodite was excluded from the measurement and analysis. Shrimp have five pairs of swimming appendages called pleopods, designated P1 through P5 from anterior (P1) to posterior (P5). Each pleopod consists of a stalklike proximal segment, called the protopodite, and a biramous distal segment formed by two hair-bearing membranes—one positioned medially, named the endopodite, and one positioned laterally, the exopodite (labeled in Fig. 1). The edges of

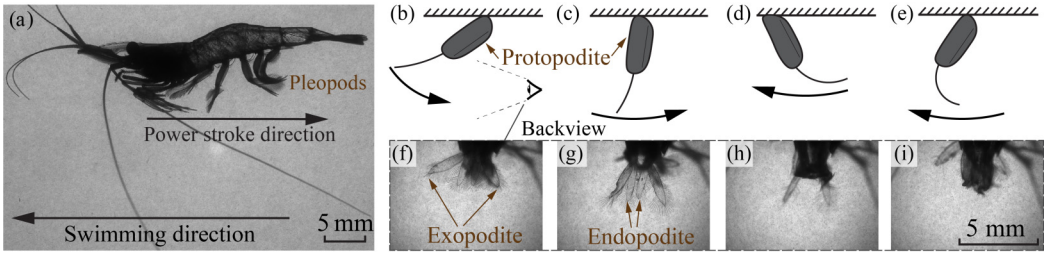

FIG. 1. (a) Representative frame from the high-speed recording of a free-swimming marsh grass shrimp. (b),(c) Pleopod motion in power stroke. (d),(e) Pleopod motion in recovery stroke. (f)–(i) The corresponding back view of the pleopods.

exopodites and endopodites are lined with fine, hairlike setae, which have low porosity [35]. The total length of the each pleopod was defined as the sum of its protopodite and exopodite lengths. Where applicable, appendage spacing was measured as the linear distance between the proximal protopodite joint of an anterior pleopod and that of its posterior neighbor. Because P5 does not have a posterior neighbor, the interpleopod distance was measured as the distance between P4 and P5. The wet weight was measured after visualization experiments with a precision balance (VWR-124B2, VWR International, USA; precision = 0.1 mg) after gently blotting excess water with paper towels, ensuring measurements did not exceed 20 s so as to prevent gill desiccation and minimize stress.

3. Side-view free-swimming experiments

Biological experiments were performed in a in a 9.5-l aquarium measuring $31.1 \times 15.9 \times 20.6\,\mathrm{cm}^3$ (internal length × width × height), with 30‰ salinity artificial seawater and a temperature of 21 °C. For free-swimming experiments, individual shrimp were brought downstream from the field of view (width≈2 BL) and within the focal plane of the camera using a beaker. The center of the tank coincided with the center of the field of view and the focal plane, yielding a clearance from the walls of about 6 BL anteriorly, 15 body widths laterally, and 10 body height vertically. We recorded scaled videos from the lateral view (corresponding to the left side of the animals) using a high-speed digital video camera (Fastcam Nova R2; Photron, Tokyo, Japan) at 2000 fps and resolution of 2048 pixels × 1472 pixels. The camera was fitted with a 60 mm macro lens (Nikon AF Micro Nikkor; Nikon, Japan) set at f/5.6. We used backlighting with an LED illuminator ($\lambda = 530$ nm, M530L2-C3; Thor Labs, Newton, NJ, USA) coupled with a collimating Fresnel lens (focal distance = 10 cm) to achieve high contrast between the shrimp appendages and the background. We first conducted a visual assessment during the experiments to identify steady swimming cases worthy of recording. We selected a single video per specimen for subsequent analyses based on specific criteria, including the clearest example of forward steady swimming and sequences where the pleopods remained within the focal plane throughout the duration of the sequence. Only the best case was used for three-dimensional (3D) reconstruction.

4. Posterior-view experiments

Scaled posterior views of the shrimp were obtained from separate experiments, involving different specimens. The shrimp were tethered to ensure a clear view of the pleopods during a full cycle. The animals were restrained at the center of the field of view using a small metal wire glued to the superior surface of the carapace. The restraint was cut as short as possible at the end of the experiments and the glue was shed during molting. Recording parameters and lighting were identical to the free-swimming cases.

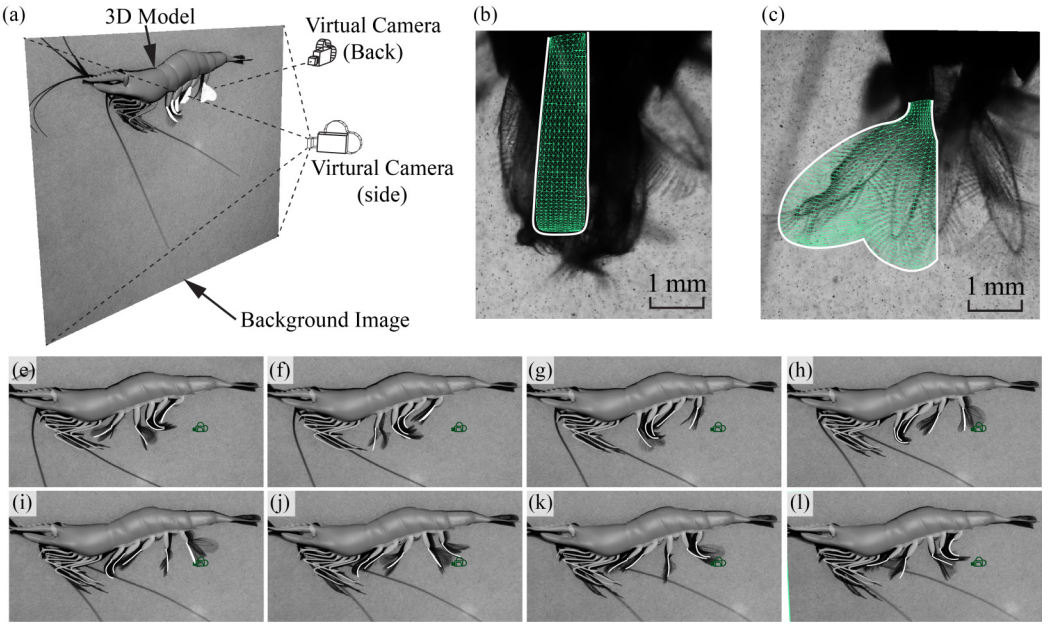

FIG. 2. (a) Virtual filming scene in autodesk maya. (b) The shape of the pleopod model at minimum area. (c) The shape of the pleopod model at maximum area. (e)–(l) Shrimp model superimposed with high-speed side-view images at eight evenly spaced time points within one period, corresponding to t/T values from 0.125 to 1. See Supplemental Material video (Movie 1 [36]).

5. Pleopod stroke cycle based on the high-speed recording

During one stroke cycle, each pleopod performs a power stroke, moving in the direction opposite to the swimming direction [Figs. 1(b) and 1(c)]. To reposition, it performs a recovery stroke, as illustrated in Figs. 1(d) and 1(e). Throughout the power stroke, the protopodites remain relatively rigid, whereas the exopodites and endopodites splay outward, causing their setae to spread and increase the effective surface area [Figs. 1(f) and 1(g)]. By contrast, when the recovery stroke begins, these distal lobes bend significantly and fold back together [Figs. 1(h) and 1(i)]. Just before the next power stroke [Fig. 1(i)], the exopodites, endopodites, and setae have fully overlapped again.

B. 3D reconstruction

We reconstructed the free-swimming shrimp into a 3D model using the software autodesk maya (Autodesk, San Raphael, CA, USA). The shrimp body and protopodites were modeled as a single entity, referred to as the "body" in the following text. The combined surface of an exopodite, endopodite, and their setae are treated as one membrane, as we also assume that these surfaces are not permeable and usually overlap [Figs. 2(b) and 2(c)]. Such membrane is modeled as a flat plate which only has longitudinal bending deformation while transverse bending is simplified. Thus, the cupping of the pleopod is not included in our model. For simplicity, the term "pleopod" will refer to this membrane that represents the surface covering the exopodite, endopodite, and their setae.

To mimic the morphing kinematics, including the exopodite's abduct-and-adduct motion and the setae's spread-out and folding motion, the area of the modeled pleopod membrane varies during the stroke. Although individual pleopods in real shrimp may differ in timing or amplitude, we apply a uniform morphing pattern across all pleopods to focus on the fundamental spread-and-fold mechanism. Figure 2(b) shows the pleopod at its minimum area, while Fig. 2(c) shows its maximum area.

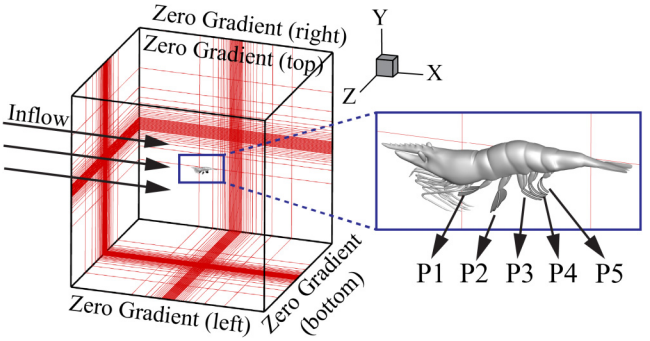

FIG. 3. Computational grid and flow domain. The five pleopods of the model are labeled as P1 to P5.

Additionally, to reconstruct the stroking kinematics, we aligned the 3D model with the background images at each time step, which were filmed by a side-view camera [Fig. 2(a)]. Since the main body of the shrimp remained relatively stable during forward swimming, the modeled main body was kept completely steady. Each pleopod is assumed to have the same period of strokes. The alignment between the shrimp model and the high-speed images at eight evenly spaced time points within a complete stroke cycle [t/T; values ranging from 0.125 to 1; Figs. 2(e)–2(l)] further supports the validity of the model, as it accurately captures the pleopod orientation and stroking dynamics over time. For further verification, a supplemental Material video (Movie 1 [36]) has been provided to showcase the detailed accuracy of the reconstructed model.

C. Numerical method and simulation setup

This study utilized the unsteady incompressible viscous Navier-Stokes equations [Eqs. (1)] as its governing equations. These equations were discretized employing a collocated grid arrangement, with primitive variables (u_i and p) stored at the cell center.

$$\frac{\partial u_i}{\partial x_i} = 0,$$
$$\frac{\partial u_i}{\partial t} + \frac{\partial (u_i u_j)}{\partial x_j} = -\frac{1}{\rho}\frac{\partial p}{\partial x_i} + \nu \frac{\partial}{\partial x_j}\left(\frac{\partial u_i}{\partial x_j}\right), \tag{1}$$

where u_i (for $i = 1, 2, 3$) denotes the velocity components in the x, y, and z directions, respectively; p is the pressure; and ρ and ν are the fluid density and kinematic viscosity, respectively.

The equations were solved by a finite-difference-based immersed-boundary method in a non-body-conforming Cartesian grid. The method used the fractional step technique for time integration. An advantage of the immersed-boundary method is its ability to avoid complicated remeshing algorithms commonly used in other conventional body-conformal methods [37]. This approach has been detailed and validated in our previous studies, ensuring the accuracy and reliability of our computational fluid dynamics solver [22,38]. The same solver has been successfully applied to investigate the mechanism of metachronal swimming [22,39–41], as well as the flow problem Reynolds numbers within range of one order of magnitude [42–46].

D. Simulation setup

During the simulation, the shrimp model is placed at the center of a flow domain with dimensions of $7.5L_b \times 7.5L_b \times 7.5L_b$ (Fig. 3). The flow domain was discretized into a grid with a size of 9.97 million nodes in total. The grid consists of three layers of mesh with different density. The densest layer of mesh has a margin close to the model which has 1.72 million nodes. This densest layer aims to cover the details of the shrimp model and nearest flow field. The second layer is less dense but

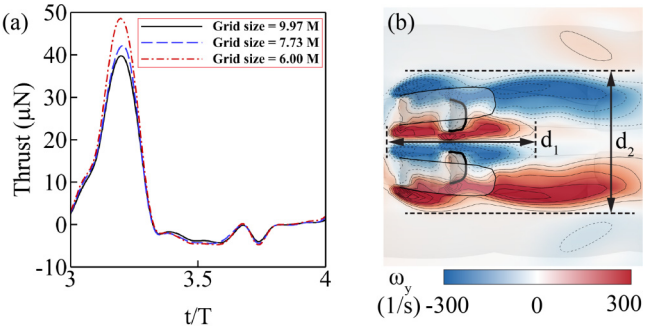

FIG. 4. (a) Grid independence study based on the instantaneous thrust of P1 during the fourth cycle; (b) cross-sectional vorticity in the y direction from a bottom view at $t/T = 3.34$. The cross-sectional locations correspond to those shown in Figs. 17(b) and 17(d). The characteristic lengths d_1 and d_2 quantify the relative changes in the edge vortices across different grid sizes.

has a larger margin which contains 7.59 million nodes. The second layer is set to be dense enough to cover the details of near field flow. The last layer is the coarsest, which serves as a smooth transition from the second layer to the domain boundary. This layer contains only 0.67 million nodes, which reduces the computational cost.

During simulations, the shrimp model was placed in the center of the flow domain, with its head pointing to the negative x direction. An inflow with constant velocity of 74.36 mm/s is given to the front boundary. The rest of the boundaries are given zero gradient boundary conditions. The body Reynolds number ($\mathrm{Re}_b = U_\infty L_b/\nu$) is 1980.10, where the kinematic viscosity ν is 1.05×10^{-6} m^2/s.

We conducted a grid independence study to ensure that the computational results achieve a balance between accuracy and computational cost. By comparing the time history of computed thrust under different grid sizes [Fig. 4(a)], we observed that as the grid size increases from 6.00 to 7.73 million, the cycle-averaged thrust decreases by 20.87%, indicating that the coarsest grid is insufficient to accurately capture the flow features. However, when the grid size is further increased from 7.73 to 9.97 million elements, the cycle-averaged thrust changes by only 4.68%, suggesting that the damping effect of grid size is largely diminished. This demonstrates that beyond a certain point, increasing the grid size has minimal impact on the accuracy of the results.

To further evaluate grid size effects on vortex structure resolution, we analyzed the relative changes in characteristic lengths (d_1 and d_2) as shown in Table II. The definitions of d_1 and d_2, along with their measurement methodology, are provided in Fig. 4(b). The coarsest grid (6.00 million) fails to accurately capture the vortex structures, as evidenced by significant deviations in d_1 and d_2. In contrast, for the intermediate and densest grids, the characteristic lengths converge, indicating that these grids provide sufficient resolution for accurate vortex representation.

Based on this analysis, the grid size of 9.97 million elements was chosen for this study as it is just sufficient to ensure the accuracy required for observing vortex structures while minimizing

TABLE II. Comparison of characteristic lengths (d_1 and d_2) to evaluate the effects of grid size on the resolution of vortex structures. The percentage indicate the relative change compared to the adjacent row with a coarser grid.

Case	Grid size (million points)	d_1 (mm)	d_2 (mm)
Densest grid (used in this study)	9.97	2.02 (+0.00%)	1.95(−1.51%)
Intermediate grid	7.73	2.02 (+100.00%)	1.98 (−5.16%)
Coarsest grid	6.00	1.01	2.11

TABLE III. Measurements of kinematics parameters. f, frequency; T, period; U_∞, swimming speed; Ψ, phase lag; $\mathrm{Re}_{\mathrm{pleo}}$, pleopod-based Reynolds number; Re_b, body Reynolds number; J, Advance ratio; St, Strouhal number.

f (Hz)	T (s)	U_∞ (mm/s)	$\Psi_{\mathrm{P1–P2}}$ (%)	$\Psi_{\mathrm{P2–P3}}$ (%)	$\Psi_{\mathrm{P3–P4}}$ (%)	$\Psi_{\mathrm{P4–P5}}$ (%)	$\Psi_{\mathrm{P5–P1}}$ (%)	$\mathrm{Re}_{\mathrm{pleo}}$	Re_b	J	St
6.27	0.16	74.36	18.44	23.13	23.13	17.81	17.53	290.48	1980.10	0.96	0.36

computational cost. All simulation results in this study are analyzed in the fourth period, which provides a steady-state solution.

III. RESULTS

A. Kinematics

As summarized in Table III, the shrimp swam at 74.36 mm/s with a beating frequency of 6.27 Hz. The average phase lag between adjacent pleopods is 20.62% T. Some nondimensional parameters are also reported in Table III, which are defined as

$$\mathrm{Re}_{\mathrm{pleo}} = \frac{\bar{U}_{\mathrm{tip}}\bar{l}_{\mathrm{pleo}}}{\nu}, \quad \mathrm{Re}_b = \frac{U_\infty L_b}{\nu}, \quad J = \frac{\bar{U}_{\mathrm{tip}}}{U_\infty}, \quad \mathrm{St} = \frac{f\bar{l}_{\mathrm{pleo}}}{U_\infty}.$$

Figure 5(a) shows the averaged time history of tip speed averaged across the five pleopods, indicating that the tip speed accelerates at the beginning of the power stroke, peaks in the middle, and drops at the end. During the recovery stroke, the acceleration is lower and more stable. At the end of the recovery stroke, the tip decelerates to zero. The mean power stroke period is 45.81% T, which is shorter than the mean recovery stroke period of 54.19% T, indicating a 15.45% faster power stroke.

Figure 5(b) shows that the tip trajectories of the five pleopods share the trend where the power stroke trajectories are positioned lower in space compared to those during the recovery stroke. This spatial asymmetry in the shrimp's stroke pattern has also been observed in other species, such as ctenophores [11,40].

Since we have modeled the pleopod surface to mimic the spread-out motion of real shrimp, the time history of normalized surface area is also calculated and reported in Fig. 6. During the power stroke, the pleopod area remains at its maximum for 15% T, while during the recovery stroke, it

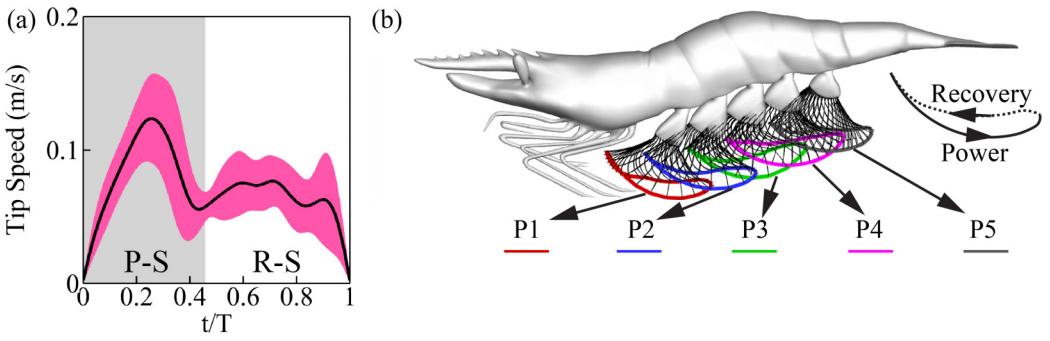

FIG. 5. (a) Averaged tip speed (black), starting from power stroke. The pink margin represents the standard deviation after removing the phase lag. The gray shaded area represents the mean power stroke period (P-S), while the unshaded area indicates the mean recovery stroke period (R-S). (b) Tip trajectory of five pleopods in one stroke period.

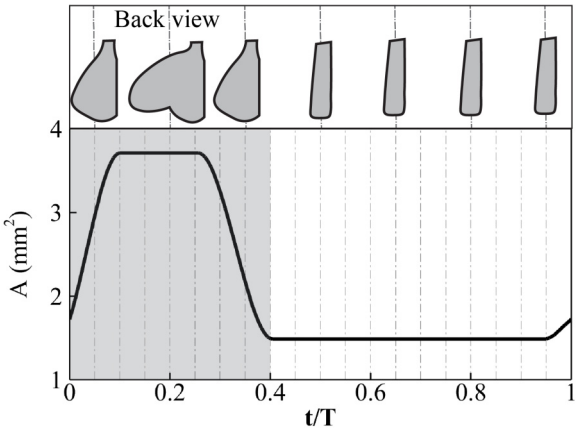

FIG. 6. Time history of the pleopod surface area, which includes the combined surfaces of the protopodite, exopodite, and setae. The top row of drawings illustrates the shape at the corresponding time. A is the pleopod surface area. The power period is shaded in gray.

stays at its minimum for 55% T. Additionally, both the spread-out and folding motions each take 10% T.

B. Baseline case—a free-swimming shrimp

The natural swimming shrimp is simulated in our in-house CFD solver, serving as the baseline case for later comparison. Figure 7(a) presents the time history of thrust force for each pleopod and their average value. Generally, every pleopod can generate positive thrust. Throughout the cycle,

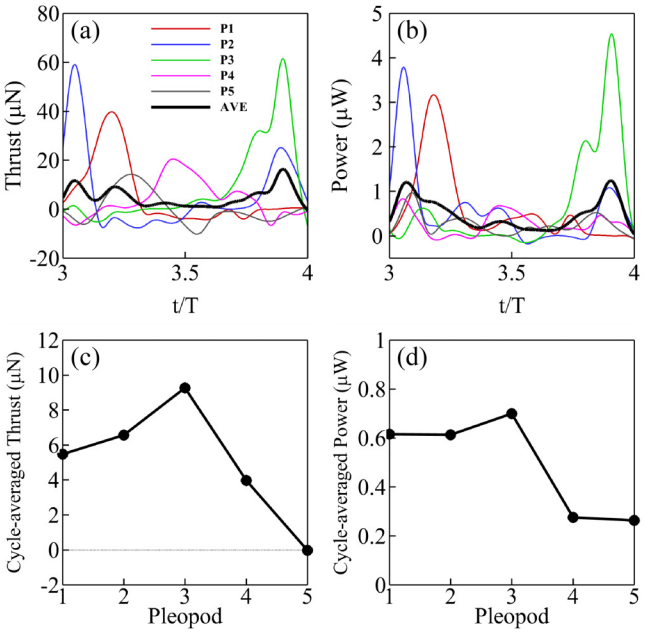

FIG. 7. (a) Time history of thrust of P1–P5 and averaged thrust. (b) Time history of hydrodynamic power of P1–P5 and averaged power. (c),(d) Cycle-averaged thrust and hydrodynamic power of each pleopod.

thrust remains mostly above zero and peaks during the power stroke, while it is mainly negative during the recovery stroke. Since these pleopods stroke under certain phase lag, when one pleopod [e.g., P2; blue in Fig. 7(a)] finishes its power stroke, the adjacent pleopod [e.g., P1; red in Fig. 7(a)] reaches its thrust peak. Such phase lag among pleopods ensures that when multiple pleopods are in the recovery stroke phase, at least one pleopod is in the power stroke phase, generating thrust. This metachronal coordination ensures that the overall thrust remains positive and stable [black in Fig. 7(a)], compared with the thrust of individual pleopods. Such stable propulsion using metachronal coordination has been observed in other species such as ctenophores [22,40].

In addition, as shown in Fig. 7(b), the time history of hydrodynamic power for each pleopod peaks during the power stroke and remains low during the recovery stroke. The averaged power consumption is also more stable than that of individual pleopods.

Figures 7(c) and 6(d) show the cycle-averaged value of thrust and hydrodynamic power for each pleopod. From the anteriormost pleopod to the posteriormost pleopod, the cycle-averaged thrust and power first increase and then decrease. From P1 to P3, the cycle-averaged thrust increases from 5.48 to 9.26 μN, an increase of 69.09%. From P3 to P4, the cycle-averaged thrust drops to 3.97 μN, a decrease of 57.17%. P5 ends up with nearly 0 cycle-averaged thrust. Figure 7(d) shows that the cycle-averaged power of P1 (0.62 μW) and P2 (0.61 μW) are nearly identical. P3 consumes 0.70 μW, which is 13.78% more than P1 and P2. The power of P4 (0.28 μW) and P5 (0.26 μW) decreases by 60.63% and 62.32%, respectively, compared to P3's power. For this baseline case, the overall cost of transport [COT = power$/(U_\infty W)$] is calculated to evaluate the overall energy cost regardless of swimming speed (U_∞) and weight (W), yielding 16.285.

Figure 8 visualizes the vortex structures that are generated by the pleopods' strokes at eight evenly spaced instants. The vortex structures are quantified by a nondimensional Q criterion ($QU_\infty^2/R^2 = 40$), which highlights regions of rotational dominance within the flow field. The visualization reveals distinct vortex sheets forming over the surfaces of the pleopods, as well as edge vortices and tip vortices resulting from flow separation at the pleopod edges. The edge vortices are observed primarily along the outer edge of the exopodites and the inner edge of the endopodites, where they remain attached for the majority of the stroke cycle. Only a small portion of the edge vortices detaches from the side edges, and when they do, they dissipate quickly in the near field without significant downstream propagation. For example, an edge vortex detached from P1 is labeled as EV1 in Fig. 8(g).

As the pleopods complete their power stroke, tip vortices generated by a pair of pleopods begin to interact and detach, forming a vortex ring in the near field. For example, at $t/T = 3.375$ [Fig. 8(d)], a new vortex ring, labeled R1, begins to form from the tip vortices generated by P1. This R1 is tracked and labeled in Fig. 8, illustrating its detachment, downstream propagation, and eventual dissipation. As the series of figures forms a loop, the progression of R1 continues beyond $t/T = 3.875$ [Fig. 8(h)] into $t/T = 3.0$ [Fig. 8(a)] and back to Fig. 8(d). At this point, the old R1, which originated in the earlier cycle, has reached the far field and is nearing dissipation. Simultaneously, a new R1 is beginning to form, illustrating how vortex ring formation and dissipation repeat over consecutive stroke cycles. Additionally, another vortex ring, R3, is labeled to highlight its distinct behavior [Fig. 8(a)]. Unlike R1, which primarily propagates downward, R3 travels more toward the back (downstream), demonstrating the variability in the direction of vortex ring propagation.

To evaluate the strength and dynamics of the induced vortex structures, Fig. 9 presents the z-direction vorticity (ω_z) at the center of two pleopod rows. During the power stroke of a pleopod pair, tip vortices are generated at the tips of the pleopods and detach as the stroke progresses. These tip vortices induce counterrotating vortices in the near field, contributing to the formation of vortex rings. As the shrimp swims, these vortices propagate backward and downward, and interactions between vortices generated by anterior and posterior pleopods create complex flow dynamics.

To illustrate this process, R1, TV1$^-$, and TV1$^+$ are labeled as examples. At $t/\mathrm{T} = 3.375$ [Fig. 9(d)], R1 begins to form with the detachment of a negatively rotating tip vortex from P1, labeled as TV1$^-$, which serves as the initial trigger for vortex ring formation. A positively rotating tip vortex, initially visible as part of a vortex sheet, detaches later and is labeled as TV1$^+$, forming a

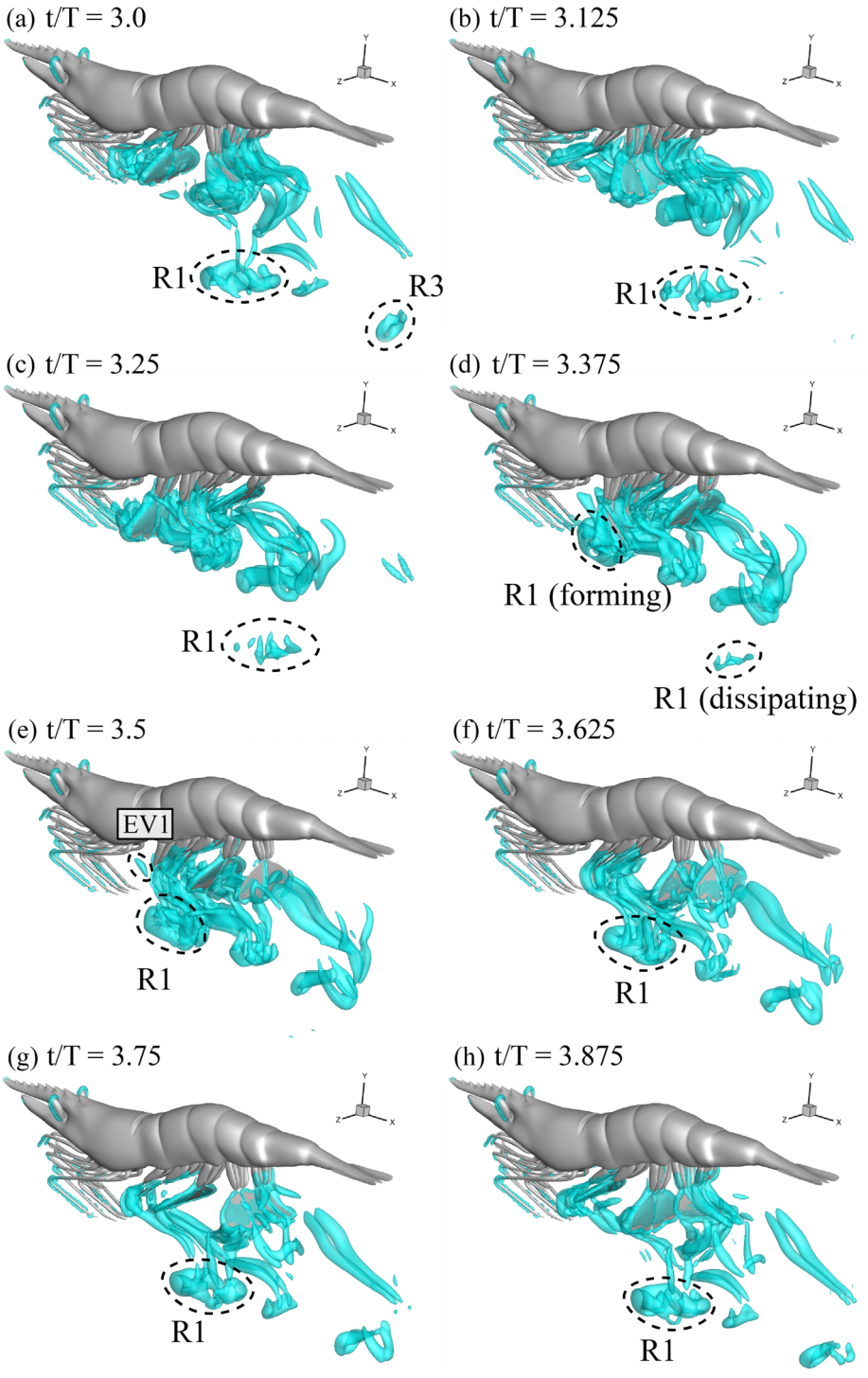

FIG. 8. (a)–(h) Vortex structures at eight evenly spaced time instants. The vortex structures are displayed based on a Q criterion ($QU_\infty^2/R^2 = 40$). R1 indicates the vortex ring formed from the tip vortices of P1, R3 indicates the vortex ring formed from the tip vortices of P3, and EV1 marks a detached edge vortex from P1. See supplemental Material video (Movie 2 [47]).

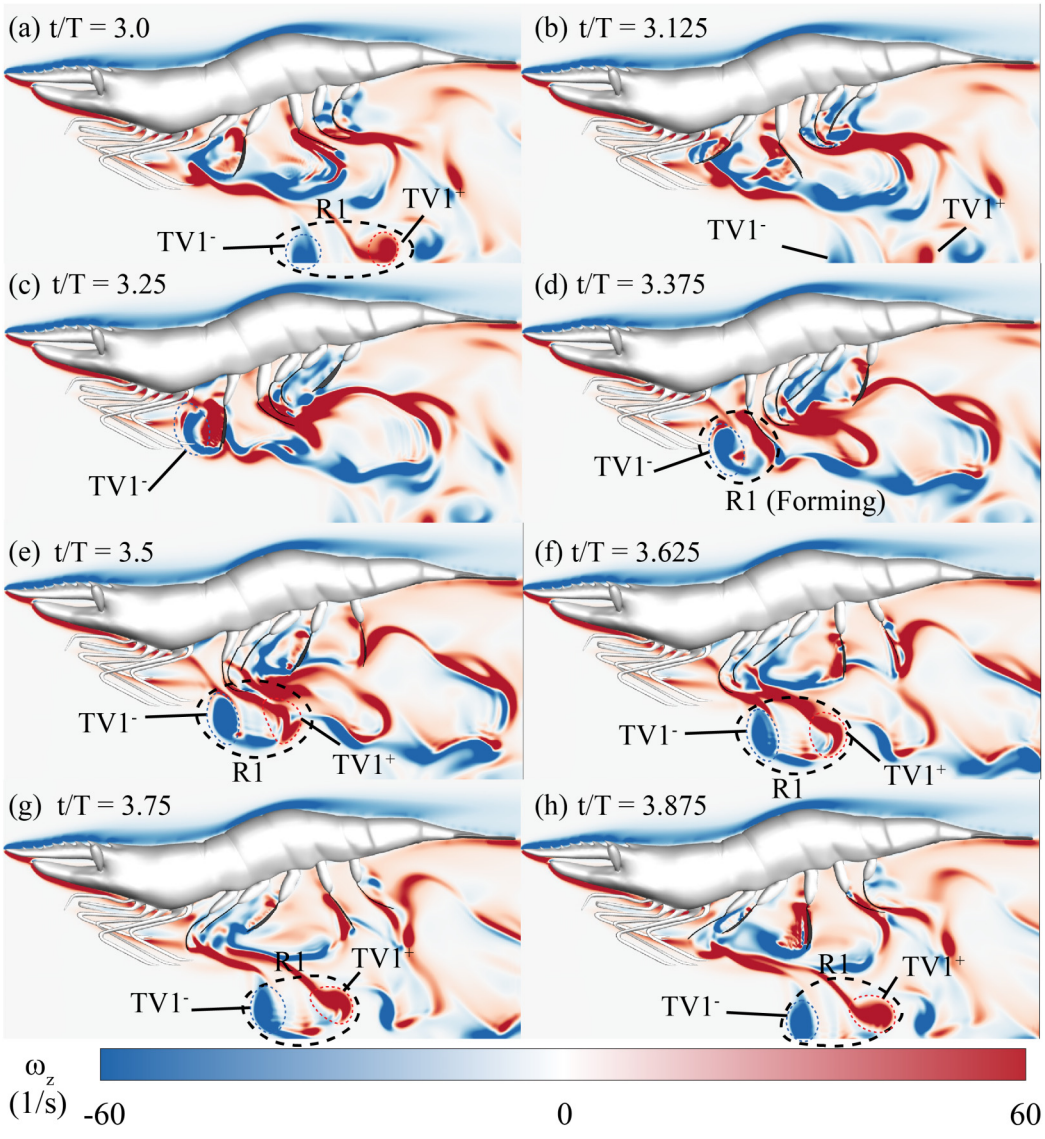

FIG. 9. (a)–(h) Cross-section view at the domain center of vorticity in the z direction (ω_z) at eight evenly spaced time instants of the fourth period. $TV1^-$ and $TV1^+$ indicate a pair of negatively and positively rotating tip vortices, respectively, which together form the vortex ring labeled as R1. See supplemental Material video (Movie 3 [48]).

pair with $TV1^-$ to complete the vortex ring R1. The progression of R1 is shown from $t/T = 3.375$ [Fig. 9(d)] through $t/T = 3.875$ [Fig. 9(h)], where it continues to propagate and develop. The series then returns to $t/T = 3.0$ [Fig. 9(a)], where R1 and its associated tip vortices propagate further downstream and downward. By $t/T = 3.375$ [Fig. 9(d)], these structures have propagated out of sight in the chosen frame but are dissipating in the far field, as previously described and shown in Fig. 8. While the underlying dynamics are similar for tip vortices generated by other pleopods, their trajectories vary depending on the pleopod's position. For example, tip vortices from more posterior

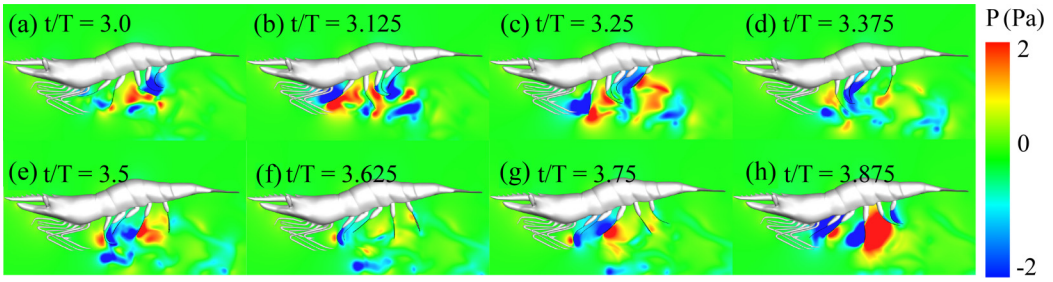

FIG. 10. Cross-section view at the domain center of instantaneous pressure fields at eight evenly spaced time steps of the fourth period.

pleopods, such as P3, tend to propagate more downstream compared to the primarily downward propagation observed for anterior pleopods like P1.

Figure 10 shows the pressure field of the baseline case from a cross-sectional side view. During the power stroke, negative pressure develops anterior to the pleopod surface, while positive pressure forms on the posterior side, contributing to thrust generation. However, during the recovery stroke, notable differences in the pressure field emerge between the anteriormost pleopod (P1) and the posterior four pleopods (P2–P5).

For the anteriormost pleopod (P1), the pressure field throughout the recovery stroke consistently exhibits positive pressure anterior to the pleopod and negative pressure posterior to it, as indicated by the pressure contours [Figs. 10(d)–10(g)]. In contrast, for the posterior pleopods (P2–P5), the anterior pressure undergoes noticeable changes during the recovery stroke. For instance, when P3 begins the recovery stroke [$t/T = 3.125$; Fig. 10(c)], the anterior pressure is positive. However, as the recovery stroke progresses, the anterior pressure becomes nearly zero [$t/T = 3.375$; Fig. 10(d)] and eventually turns negative [$t/T = 3.375$; Fig. 10(e)]. Despite these variations in anterior pressure, the posterior pressure for P2–P5 remains consistently negative, similar to that of P1. Farther beneath the pleopods, small negative and positive pressure zones can also be observed due to the dissipation and interaction among attached vortices.

Shifting focus from the pressure field, Figs. 11(a)–11(e) present the thrust distribution for each pleopod at eight evenly spaced instants during a swimming cycle, illustrating how pressure differences across the pleopod surfaces generate thrust. The thrust, defined as the horizontal component of the total force, arises from the pressure difference across the pleopod surfaces, integrated with respect to area. During the power stroke, thrust is predominantly generated in the lower half region

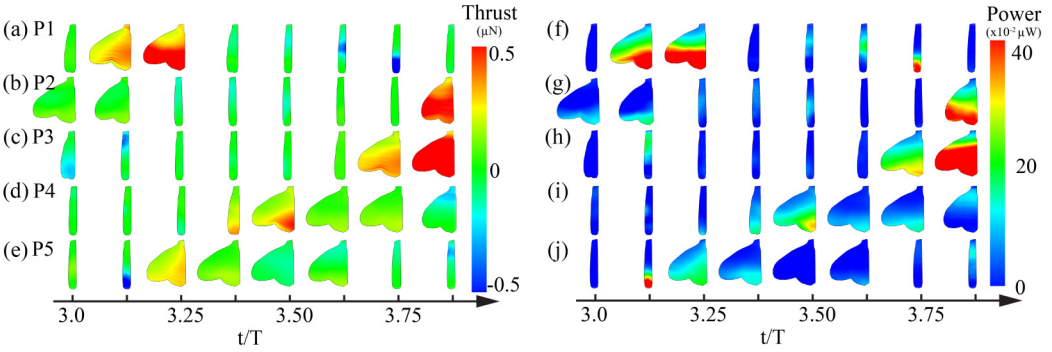

FIG. 11. (a)–(e) Surface thrust distribution of P1 to P5 at eight evenly spaced time instants of the period. (f)–(j) Surface power (Pw) distribution of P1 to P5 at eight evenly spaced time instants of the fourth stroke cycle.

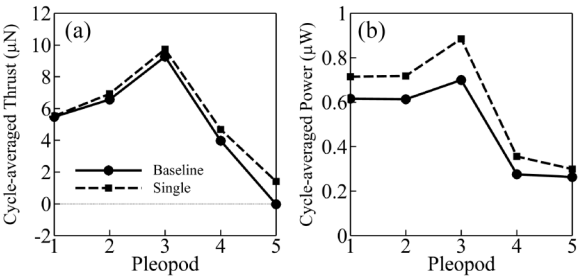

FIG. 12. Cycle-averaged (a) thrust, (b) hydrodynamic power of the baseline case and single-pleopod cases

of the pleopods. In contrast, during the recovery stroke, when drag is encountered, the forces are primarily concentrated at the tips of the pleopods.

Corresponding to the thrust distribution, the distribution of hydrodynamic power is shown in Figs. 11(f)–11(j). During the power stroke, power is consumed in the lower half region, while during the recovery stroke, power is consumed on the tip. This observation reveals the different ways that power is consumed by the power and recovery stroke.

The above analysis has focused on characterizing the flow dynamics of a freely swimming shrimp, providing a baseline understanding of how the pleopods generate thrust and encounter drag. While these observations offer valuable insights into the mechanics of shrimp locomotion, the primary objective of this study is to investigate the collaborative effects of the pleopods. Specifically, we aim to assess how metachronal coordination among pleopods enhances swimming performance compared to the case where pleopods operate independently. This comparison is explored in the subsequent sections.

C. Cases with single pair of pleopods

To quantitatively study the interpleopod interactions, we conduct five additional simulations using models that only have one pleopod pair, under the same flow conditions, to compare with the baseline model. By doing so, each pleopod in the baseline case can be compared with the corresponding pleopod in single-pleopod cases. In Fig. 12, the cycle-averaged thrust and power are compared between the baseline and single-pleopod cases, which are also listed in Table IV.

TABLE IV. Cycle-averaged thrust, power, propulsion efficiency (η) and cost of transport (COT) for the baseline and single-pleopod cases. The propulsion efficiency and cost of transport are calculated over all pleopods.

Cases	No.	Cycle-averaged thrust (μN)	Cycle-averaged power (μW)	η	COT
	P1	5.48	0.615		
	P2	6.57	0.613		
Baseline	P3	9.26	0.700	76.03%	16.295
	P4	3.97	0.276		
	P5	−0.03	0.264		
	P1	5.52	0.715		
	P2	6.93	0.718		
Single	P3	9.73	0.885	70.71%	19.627
	P4	4.68	0.356		
	P5	1.41	0.300		

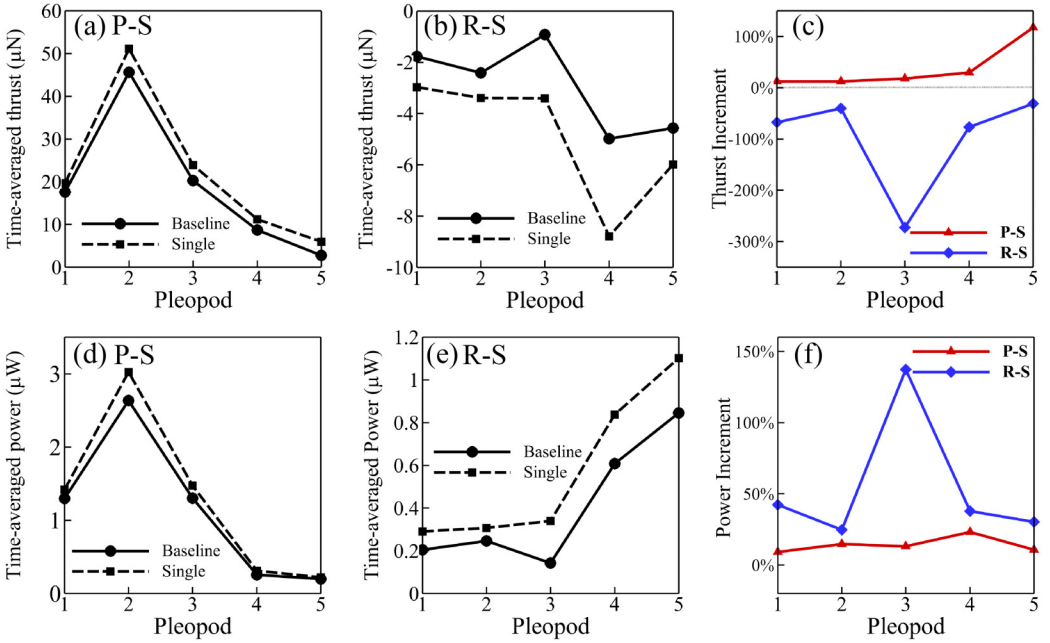

FIG. 13. (a),(b) Time-averaged thrust of the baseline and single-pleopod case during power stroke (P-S) and recovery stroke (R-S). (c) Thrust increments of the single-pleopod regarding the baseline case. (d),(e) Time-averaged power of the baseline and single-pleopod case during P-S and R-S. (f) Power increments of the single-pleopod regarding the baseline case.

The cycle-averaged thrust of the baseline case, averaged over five pleopods, is 5.05 μN, which is 10.70% less than the averaged value of five single-pleopod cases, 5.66 μN. However, the cycle-averaged power of the baseline case, averaged over five pleopods, is 0.49 μW, which is 19.46% less than the 0.59 μW of the five single-pleopod cases. Furthermore, the propulsion efficiency ($\eta = \text{thrust} \times U_\infty/\text{power}$) and the cost of transport for the five pleopods are also calculated and summarized in Table IV. In summary, the baseline case only produces around 10% less thrust but saves up to nearly 20% power compared to the single-pleopod cases.

Furthermore, evaluating the performance of the power and recovery strokes separately is crucial, as the cycle-averaging process negates the thrust generated during the power stroke with the drag incurred during the recovery stroke. This averaging diminishes the visibility of interappendage interactions and their specific impacts on each stroke phase. To address this, the time-averaged thrust in power and recovery stroke is shown separately in Figs. 13(a) and 12(b), and the time-averaged power is shown separately in Figs. 13(d) and 12(e).

During the power stroke, the time-averaged thrust and power between the baseline and single-pleopod cases are relatively similar [Figs. 13(a) and 13(d)], with the power increase from the baseline to the single-pleopod cases ranging from 9.25% to 23.22%. However, more pronounced differences emerge during the recovery stroke. The increases in drag from the baseline case to the single-pleopod cases range from 31.19% up to 272.94% [Fig. 13(b)]. These phase-specific thrust and drag increments for each pleopod are further detailed in Fig. 13(c), illustrating that the drag increment during the recovery stroke is consistently more significant than the thrust increment during the power stroke. Notably, P3 exhibits the highest drag increment among the pleopods during the recovery stroke.

Moreover, the comparison for power consumption shows a similar trend to the comparison for thrust. The difference in power consumption between the two cases is much larger during the

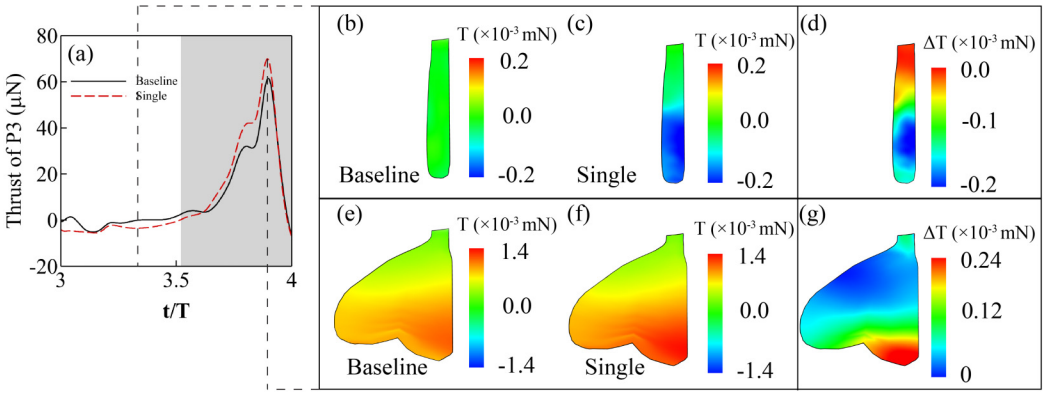

FIG. 14. (a) Time history of the thrust of P3 in the baseline and single-pleopod cases. (b),(c) Thrust distribution on the pleopods at $t/T = 3.34$. (d) The distribution of thrust difference (Thrust of the single-pleopod case minus that of the baseline case) at $t/T = 3.34$. (b),(c) Thrust distribution on the pleopods at $t/T = 3.90$. (d) The distribution of thrust difference (Thrust of the single-pleopod case minus that of the baseline case) at $t/T = 3.90$.

recovery stroke than during the power stroke, with the power consumption of P3 in the single-pleopod case increasing by 137.30% compared to the baseline case [Figs. 13(e) and 13(f)].

The larger drag and power consumption increments observed for P3 indicate that its performance is strongly influenced by interpleopod interactions, suggesting enhanced effectiveness when operating within the baseline coordinated system. This observation will be further discussed in the context of vortex dynamics and body curvature effects in the discussion section.

In summary, the baseline's performance during the power stroke is only slightly better than that of the single-pleopod case. However, during the recovery stroke, the baseline performs much better, with P3 producing 272.94% less drag and consuming 137.30% less power.

Due to the prominent effect of inter-pleopod interactions on P3, it is selected for further comparison in the following analysis. Figure 14(a) compares the P3's time history of thrust, showing that the baseline case produces reduced drag during the recovery stroke and reduced thrust during the power stroke. Figures 14(b) and 14(c) show the thrust distribution at one instant during the recovery stroke, while Figs. 14(e) and 14(f) show another instant during the power stroke. By subtracting values in baseline case from the single-pleopod case, Fig. 14(d) shows that, during the recovery stroke, the major reduction of drag in the baseline case occurs in the lower half region of the pleopod. During the power stroke, as shown in Fig. 14(g), the major reduction of thrust is also distributed at the tip, specifically at the endopodite's tip.

A similar comparison is conducted for hydrodynamic power at the same instants, with the time history of power for the two cases calculated (Fig. 15). In both power and recovery stroke, as shown in Fig. 15(a), the power in the single-pleopod case is higher than in the baseline case throughout the whole cycle. Similarly, Figs. 15(d) and 14(g) show the distribution of power differences between the two cases, indicating how much more power the single-pleopod case consumes compared to the baseline case. Similar to the thrust distribution, the excess power consumption in the single-pleopod case is concentrated at the tip region of the endopodites.

Such effect of an interappendage interaction on thrust and power performance is suspected to result from the affected pressure field near the pleopod surfaces, particularly the pressure gradient across the pleopods. To investigate this hypothesis, Fig. 16 compares the pressure field for two cases at the selected instant during recovery stroke. As P3 performs the recovery stroke, the pressure anterior to P3 in the single-pleopod case is higher than in the baseline case, while the pressure posterior to P3 is similar in both cases [Figs. 16(a), 16(b) and 15(e), 15(f)]. This indicates that P3 in the single-pleopod case creates a larger pressure gradient across its surface. Figures 16(c),

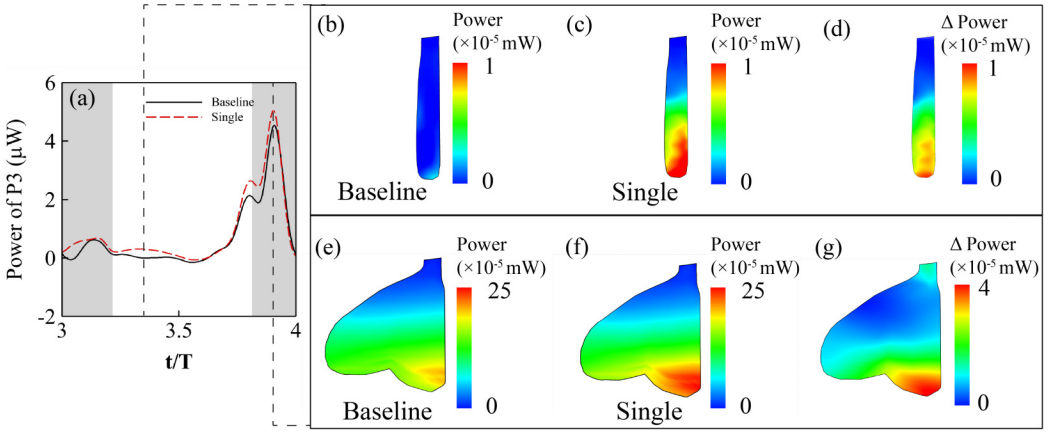

FIG. 15. (a) Time history of the hydrodynamic power of P3 in the baseline and single-pleopod cases. (b),(c) Power distribution on the pleopods at $t/T = 3.34$. (d) The distribution of power difference (Thrust of the single-pleopod case minus that of the baseline case) at $t/T = 3.34$. (b),(c) Thrust distribution on the pleopods at $t/T = 3.90$. (d) The distribution of power difference (power of the single-pleopod case minus that of the baseline case) at $t/T = 3.90$.

15(d), 15(g), and 15(h) show the pressure distribution on both the anterior and the posterior surface, validating this corollary. These observations indicate that the interaction reduces the surface pressure on the anterior side of the pleopod, weakening the pressure gradient and thereby reducing drag during the recovery stroke.

Such difference of pressure field in both cases may result from the observed vortex interactions. To further explore this, Fig. 17 compares the vorticity and velocity fields, similarly at t/T of 3.34. In Fig. 17(a), a tip vortex attached to P3 (TV3) is not formed in the baseline case. Comparing to the unformed TV3 in the baseline case, Fig. 17(c) shows that TV3 is formed and attached to P3 in the single-pleopod case. Such difference indicates the interappendage interactions prevent the formation of tip vortices and weaken the tip vortices. Moreover, Fig. 17(a) shows that the velocity vectors

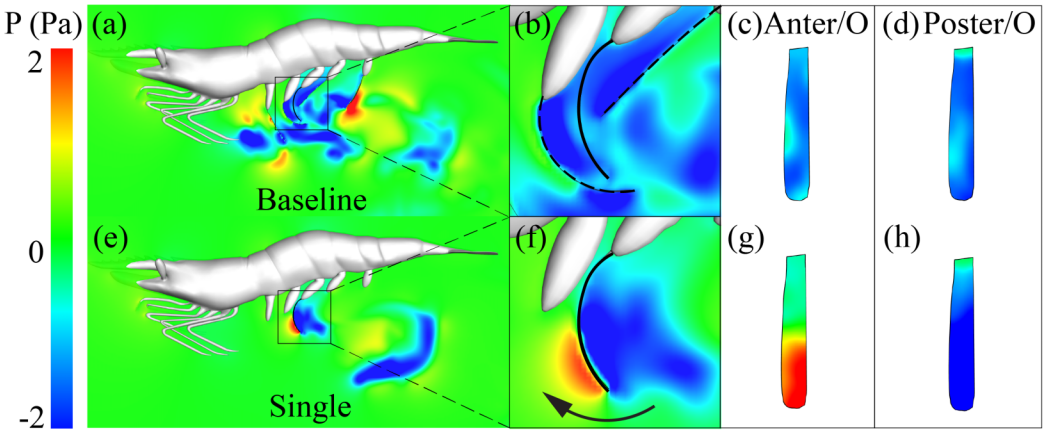

FIG. 16. Baseline case: (a) Cross-sectional pressure field across the P3 endopodite at $t/T = 3.34$, and (b) its zoom-in view, with the according surface distribution on the (c) anterior surface and (d) posterior surface. Single-pleopod case: (e) Cross-sectional pressure field across the P3 endopodite at $t/T = 3.34$, and (f) its zoom-in view, with the according surface distribution on the (g) anterior surface and (h) posterior surface.

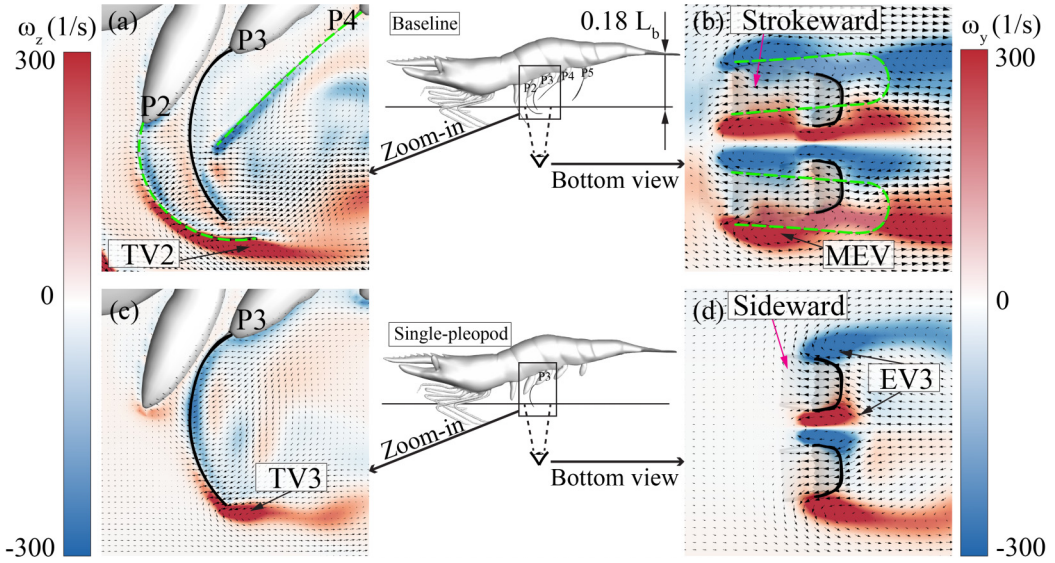

FIG. 17. Baseline case: (a) Cross-sectional vorticity in the z direction in the side view and (b) cross-sectional vorticity in the y direction in the bottom view. Single-pleopod case: (c) Cross-sectional vorticity in the z direction in the side view and (d) cross-sectional vorticity in the y direction in the bottom view. The black solid lines indicate the boundary of pleopod P3, while the yellow-green dashed lines represent the boundaries of the other pleopods. EV, edge vortex; TV, tip vortex; MEV, merged edge vortex. Supplemental Material movies from the side view [Movies 4(a) and 4(b) [49,50]] and bottom view [Movies 5(a) and 5(b) [51,52]] are provided to illustrate the pleopod motion and the generation of vortices in greater detail.

anterior to P3 in the baseline case point more towards the anterior, aligning with the direction of P3's recovery stroke. However, in Fig. 17(c), the velocity vectors anterior to P3 in the single-pleopod case direct more downward, with the tip vortex formed. Thus, such effects on flow direction between pleopods may be reasonably related to the tip vortex.

However, Fig. 14(d) has suggested that the interappendage interaction affects a broader region than just the tip, specifically extending to the entire lower half region. Thus, it is speculated that the edge vortices may contribute more to the effects on flow direction between pleopods. In the single-pleopod case [Fig. 17(d)], P3 generates a single pair of edge vortices (EV3) on its inner and outer side edges. In the baseline case [Fig. 17(b)], a similar EV3 is generated by P3. However, this EV3 merges with another pair of edge vortices generated by P2, instead of circulating alone. During the recovery stroke, due to the closer distance of the two adjacent pleopods, these two pairs of edge vortices merge, forming a pair of larger vortices. The merged edge vortex (MEV) extends enough to cover the space between the side edges of P2 and P3. Examining the velocity field of the baseline case, under the influence of the countercirculating pair of MEVs, the velocity between P2 and P3 is directed more anteriorly, aligning with the recovery stroke direction. In contrast, the velocity anterior to P3 in the single-pleopod case is either directed sideward or has a trivial magnitude. This observation reveals that the interappendage interaction induces the merging of adjacent edge vortices, redirecting the velocity anterior to the pleopod strokeward. This induced anterior flow can reduce the pressure on the pleopod's anterior surface, again, reducing drag during the recovery stroke.

IV. DISCUSSION

Our simulation results showed that shrimp swimming with a single-pleopod pair experienced a 20.46% increase in the COT compared to those with pairs of pleopods working independently, while the overall thrust increased by only 11.98%. The primary mechanism behind this power reduction

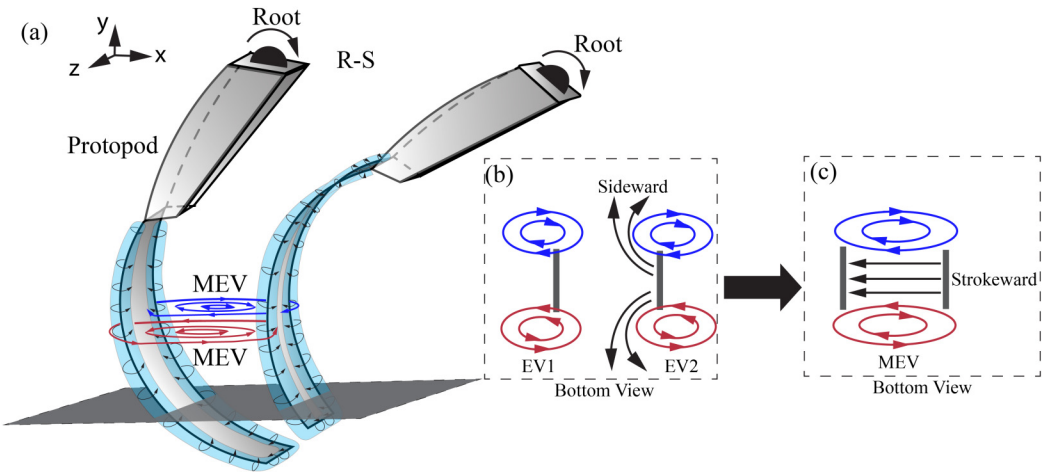

FIG. 18. Illustration of interpleopod interaction: interappendage strokeward flow inducement. (a) 3D illustration. (b) Cross-section bottom view when two pleopods are far apart. (c) Cross-section view when two pleopods get close. EV, edge vortex; MEV, merged edge vortex.

is the drag reduction during the recovery stroke, caused by a decrease in pressure anterior to the pleopods. This pressure reduction is attributed to a flow inducement resulting from the interaction between the edge vortices of adjacent pleopods. As the pleopods approach each other during the recovery stroke, these edge vortices merge into larger vortices that span across the edges of two pleopods, as illustrated in Fig. 18(a). Initially, when the pleopods are not yet sufficiently close, the edge vortices draw the flow sideward [Fig. 18(b)]. However, once the pleopods get close enough, the merged edge vortices exert a more pronounced influence, aligning the flow direction with its stroke direction [Fig. 18(c)]. Such strokeward flow inducement between adjacent pleopods, in turn, diminishes the pressure ahead of the posterior pleopod's surface, thereby reducing drag.

The strokeward flow inducement between two pleopods during the recovery stroke weakens the formation of tip vortices on the posterior pleopod. This weakening occurs due to the reliance of tip vortex formation on the pressure gradient across the tip. Typically, when only one pleopod is stroking, a pronounced pressure gradient exists between the anterior and posterior surfaces of the tip region, facilitating the formation of the tip vortex. However, strokeward flow inducement diminishes this pressure gradient, weakening the formation process. This vortex weakening mechanism has also been observed in our previous study of ctenophores, where the phenomenon occurred under Reynolds numbers (Re) ranging from 7.5 to 120 and vanished as Re increased [22]. In comparison, the current shrimp study was conducted under a much higher Re of 1980, yet this vortex weakening phenomenon was still observable, suggesting that the shrimp swimming extend the upper limit of Re for its occurrence. The extension of the Re range for the phenomenon should be attributed to the reduced distance between pleopod surfaces. During some moments of the recovery stroke, adjacent pleopods coalesce due to their partial synchronized motions, shortening the distance between pleopods' surfaces and forming a tight group. This observation further supports the theory that although the vortex-weakening mechanism is more likely to occur at lower Re and less so at higher Re, the upper limit of Re for its occurrence may be extended to higher values by decreasing appendage spacing [22]. When optimizing the design of metachronal paddling robots, if the vortex weakening mechanism is challenging to induce due to reaching the upper limit of Re for its occurrence, shorter appendage spacing should be considered. This adjustment can potentially extend the upper limit of Re for the phenomenon to take place.

Additionally, the effective area of the drag reduction mechanism can be adjusted by the appendage spacing. During the recovery stroke, the posterior pleopod tilts towards the anterior

pleopod to follow its motion. Consequently, the posterior pleopod forms a smaller angle against the abdomen compared to the anterior pleopod, causing a misalignment of their tips. This misalignment, compounded by the kinematics and deformation, results in the tip distance being smaller than the root distance between the anterior and posterior pleopods. As a consequence of this misalignment, only a distal portion of the posterior pleopod comes into close proximity to interact with the anterior pleopod. This specific area where interaction occurs can be termed the "interacting area." In the current shrimp model, it is observed that only the lower half surface of the posterior pleopod interacts with the anterior pleopod, leading to drag reduction primarily in the lower half of the follower pleopod [Fig. 14(d)]. Modifying the root spacing can either expand or contract the interacting area, thereby influencing the effectiveness of the drag reduction mechanism. For instance, increasing the root spacing extends the drag reduction mechanism towards more distal areas, consequently reducing the interacting area. Therefore, engineering designs can adjust the interacting area simply by adjusting the root spacing and bending deformations.

The observation that P3 exhibits the largest drag and power consumption increments when operating independently indicates that it benefits the most from interpleopod interactions in the baseline metachronal coordination. This suggests that certain factors may amplify these interactions. One possible explanation is P3's central position within the row of pleopods in the metachronal coordination, where its relative location might expose it to stronger vortex interactions generated by the pleopods on either side. Another contributing factor could be the shrimp's arched body curvature, with the root of P3 positioned highest among the pleopods, potentially enhancing the angle of vortex interactions. Similar effects have been observed in ctenophores [22], where body curvature pivots the total force direction to increase the thrust component. While this study lacks direct evidence to confirm these mechanisms, future work could explore the roles of relative pleopod positioning and body curvature in amplifying interpleopod interactions to provide deeper insights into shrimp locomotion.

While our findings provide valuable insights into understanding the mechanism of how interappendage interaction leads to drag reduction, it is crucial to acknowledge the limitations of this mechanism. Our analysis and discussion primarily center on the recovery stroke, during which the pleopods are in close proximity, facilitating edge vortex interaction. However, our current analysis does not adequately address whether this interaction persists during the power stroke when the distance between pleopod tips increases. Nevertheless, our results suggest that a similar force reduction mechanism may affect the power stroke, albeit to a lesser extent. This inference is drawn from the observed reduction in peak thrust during the power stroke due to interpleopod interaction. We suspect that this thrust reduction is a consequence of edge vortex interaction, wherein the merging of edge vortices induces a strokeward flow that decreases pressure behind the pleopods. This pressure reduction diminishes the pressure differential between the posterior and anterior surfaces, leading to thrust reduction. Furthermore, our findings indicate that this thrust reduction during the power stroke is more than three times less significant than the drag reduction observed in the recovery stroke, implying a limited impact on overall thrust performance. This discrepancy may be attributed to the propulsion mechanism of metachronal swimming, which relies on suction force, with the low-pressure zone in front of appendages playing a crucial role in thrust production during the power stroke [12]. In contrast, the strokeward flow inducement primarily affects the pressure behind the appendages, making it less effective on thrust production. Consequently, the strokeward flow inducement naturally has a greater impact on the recovery stroke than the power stroke. Future studies could delve deeper into the interaction of edge vortices and strokeward flow inducement to explain why interappendage interactions negatively affect thrust production during the power stroke.

Moreover, the use of a single representative shrimp morphology and behavior model introduces limitations due to biological variability. Differences in pleopod size, shape, swimming speed, flexibility, and movement patterns across individuals and species could influence the strength and dynamics of these interactions. However, the primary observation of strong edge vortex interactions remains robust, as it is grounded in the underlying fluid mechanics of multipleopod-driven flows. Future studies incorporating diverse morphological, kinematic, and behavioral models could further

explore how interspecies variability impacts vortex dynamics, offering deeper insights into the universality of these findings. Additionally, the study was conducted at a specific Reynolds number representative of the natural swimming conditions for the studied species. At lower Reynolds numbers, such as those relevant to ctenophores, the effects of edge vortex interactions may differ from those observed in this study. At much higher Reynolds numbers, the influence of viscous effects diminishes, also potentially altering the vortex dynamics.

In addition to the discussed effects of interappendage interaction on tip vortex formation, future research could aim to elucidate its impact on the detachment of tip vortices. As previously discussed, the strokeward flow inducement weakens the formation of tip vortices, potentially leading to a delay in their detachment. Given that the direction of detached tip vortices relies on the tip velocity direction at detachment, delayed detachment may alter their travel trajectories. Notably, studies have indicated that closer appendage spacing, indicative of stronger interappendage interaction, results in more horizontally traveling tip vortices [29]. By using the findings in this study to evaluate the interaction effects on detached vortices, future research may provide deeper insight into the underlying mechanisms of those interactions among detached vortices.

V. CONCLUDING REMARKS

In this study of forward metachronal swimming, our numerical results show that shrimps would encounter a 20.46% increase in the cost of transport without interappendage interactions. The interaction has been demonstrated to have a significant effect on drag reduction during recovery stroke. The baseline case encountered 272.94% less drag and 137.30% less hydrodynamic power consumption than the single-pleopod case during the recovery stroke. The primary mechanism behind this is the decrease in pressure anterior to the pleopods while the posterior surface pressure remains the same. This pressure gradient reduction is attributed to a flow inducement resulting from the interaction between the edge vortices attached to adjacent pleopods, which merge during the recovery stroke. The merged edge vortices span across the edges of two pleopods, aligning the direction of flow anterior to the pleopod with its stroke direction. This strokeward flow inducement diminishes the pressure on the pleopod's anterior surface, causing drag reduction.

ACKNOWLEDGMENTS

This work was supported by funding from the National Science Foundation to C.L. (CBET-2451990) and the Brown University Office of the Vice President for Research awarded to M.M.W. (OVPR SEED-GR300268).

[1] K. Garayev and D. W. Murphy, Metachronal swimming of mantis shrimp: Kinematics and interpleopod vortex interactions, Integr. Comp. Biol. **61**, 1631 (2021).

[2] M. Ruszczyk, D. R. Webster, and J. Yen, Trends in stroke kinematics, Reynolds number, and swimming mode in shrimp-like organisms, Integr. Comp. Biol. **62**, 791 (2022).

[3] M. P. Ford, W. J. Ray, E. M. DiLuca, S. N. Patek, and A. Santhanakrishnan, Hybrid metachronal rowing augments swimming speed and acceleration via increased stroke amplitude, Integr. Comp. Biol. **61**, 1619 (2021).

[4] N. B. Tack, S. O. Santos, and M. M. Wilhelmus, Going around the bend to understand the role of leg coalescence in metachronal swimming, Biorxiv (2024).

[5] D. W. Murphy, D. R. Webster, S. Kawaguchi, R. King, and J. Yen, Metachronal swimming in Antarctic krill: Gait kinematics and system design, Mar. Biol. **158**, 2541 (2011).

[6] M. P. Ford and A. Santhanakrishnan, On the role of phase lag in multi-appendage metachronal swimming of euphausiids, Bioinspir. Biomim. **16**, 066007 (2021).
[7] M. P. Patria and K. Wiese, Swimming in formation in krill (Euphausiacea), a hypothesis: Dynamics of the flow field, properties of antennular sensor systems and a sensory–motor link, J. Plankton Res. **26**, 1315 (2004).
[8] S. L. Tamm, Cilia and the life of ctenophores, Invertebr. Biol. **133**, 1 (2014).
[9] W. L. Heimbichner Goebel, S. P. Colin, J. H. Costello, B. J. Gemmell, and K. R. Sutherland, Scaling of ctenes and consequences for swimming performance in the ctenophore *Pleurobrachia bachei*, Invertebr. Biol. **139**, e12297 (2020).
[10] A. Dauptain, J. Favier, and A. Bottaro, Hydrodynamics of ciliary propulsion, J. Fluids Struct. **24**, 1156 (2008).
[11] A. Herrera-Amaya, E. K. Seber, D. W. Murphy, W. L. Patry, T. S. Knowles, M. M. Bubel, A. E. Maas, and M. L. Byron, Spatiotemporal asymmetry in metachronal rowing at intermediate Reynolds numbers, Integr. Comp. Biol. **61**, 1579 (2021).
[12] S. P. Colin, J. H. Costello, K. R. Sutherland, B. J. Gemmell, J. O. Dabiri, and K. T. Du Clos, The role of suction thrust in the metachronal paddles of swimming invertebrates, Sci. Rep. **10**, 17790 (2020).
[13] J. Daniels, N. Aoki, J. Havassy, K. Katija, and K. J. Osborn, Metachronal swimming with flexible legs: A kinematics analysis of the midwater polychaete *Tomopteris*, Integr. Comp. Biol. **61**, 1658 (2021).
[14] E. W. Knight-Jones and A. Macfadyen, The metachronism of limb and body movements in annelids and arthropods, in *Proceedings of the 15th International Congress of Zoology* (International Congress of Zoology, 1959), pp. 969–971.
[15] S. P. Colin, J. H. Costello, L. J. Hansson, J. Titelman, and J. O. Dabiri, Stealth predation and the predatory success of the invasive ctenophore *Mnemiopsis leidyi*, Proc. Natl. Acad. Sci. USA **107**, 17223 (2010).
[16] M. L. Byron *et al.*. Metachronal motion across scales: Current challenges and future directions, Integr. Comp. Biol. **61**, 1674 (2021).
[17] S. Michelin and E. Lauga, Efficiency optimization and symmetry-breaking in a model of ciliary locomotion, Phys. Fluids **22**, 111901 (2010).
[18] A. Ghorbani and A. Najafi, Symplectic and antiplectic waves in an array of beating cilia attached to a closed body, Phys. Rev. E **95**, 052412 (2017).
[19] S. Chateau, J. Favier, S. Poncet, and U. D'Ortona, Why antiplectic metachronal cilia waves are optimal to transport bronchial mucus, Phys. Rev. E **100**, 042405 (2019).
[20] S. Alben, K. Spears, S. Garth, D. Murphy, and J. Yen, Coordination of multiple appendages in drag-based swimming, J. R. Soc. Interface **7**, 1545 (2010).
[21] M. P. Ford, H. K. Lai, M. Samaee, and A. Santhanakrishnan, Hydrodynamics of metachronal paddling: Effects of varying Reynolds number and phase lag, R. Soc. Open Sci. **6**, 191387 (2019).
[22] S. Lionetti, Z. Lou, A. Herrera-Amaya, M. L. Byron, C. Li, S. Lionetti, Z. Lou, A. Herrera-Amaya, M. L. Byron, and C. Li, A new propulsion enhancement mechanism in metachronal rowing at intermediate Reynolds numbers, J. Fluid Mech. **974**, A45 (2023).
[23] D. E. Alexander, Kinematics of swimming in two species of *Idotea* (Isopoda: Valvifera), J. Exp. Biol. **138**, 37 (1988).
[24] M. J. Morris, G. Gust, and J. J. Torres, Propulsion efficiency and cost of transport for copepods: A hydromechanical model of crustacean swimming, Mar. Biol. **86**, 283 (1985).
[25] L. A. Van Duren and J. J. Videler, Escape from viscosity: The kinematics and hydrodynamics of copepod foraging and escape swimming, J. Exp. Biol. **206**, 269 (2003).
[26] E. I. Lamont and R. B. Emlet, Swimming kinematics of cyprids of the barnacle *Balanus glandula*, Integr. Comp. Biol. **61**, 1567 (2021).
[27] E. I. Lamont and R. B. Emlet, Permanently fused setules create unusual folding fans used for swimming in cyprid larvae of barnacles, Biol. Bull. **235**, 185 (2018).
[28] K. Kohlhage and J. Yager, An analysis of swimming in remipede crustaceans, Philos. Trans. R. Soc., B **346**, 213 (1994).
[29] M. P. Ford and A. Santhanakrishnan, Closer appendage spacing augments metachronal swimming speed by promoting tip vortex interactions, Integr. Comp. Biol. **61**, 1608 (2021).

[30] D. Kim and M. Gharib, Characteristics of vortex formation and thrust performance in drag-based paddling propulsion, J. Exp. Biol. **214**, 2283 (2011).
[31] K. Taira and T. Colonius, Three-dimensional flows around low-aspect-ratio flat-plate wings at low Reynolds numbers, J. Fluid Mech. **623**, 187 (2009).
[32] D. W. Murphy, D. R. Webster, and J. Yen, The hydrodynamics of hovering in Antarctic krill, Limnol. Oceanogr. Fluids Environ. **3**, 240 (2013).
[33] Bokeon Kwak and Joonbum Bae, Locomotion of arthropods in aquatic environment and their applications in robotics, Bioinspir. Biomim. **13**, 041002 (2018).
[34] S. Oliveira Santos, N. Tack, Y. Su, F. Cuenca-Jiménez, O. Morales-Lopez, P. A. Gomez-Valdez, and M. M. Wilhelmus, Pleobot: A modular robotic solution for metachronal swimming, Sci. Rep. **13**, 9574 (2023).
[35] Mageean Brown, Sara Oliveira Santos, Nils B. Tack, and Monica M. Wilhelmus, Analysis of shrimp appendage cupping on swimming performance through a bio-inspired model, in *76th Annual Meeting of the Division of Fluid Dynamics* (American Physical Society, 2023).
[36] See Supplemental Material at http://link.aps.org/supplemental/10.1103/PhysRevFluids.10.043103 for the reconstructed metachronal motion of the shrimp model within one period.
[37] R. Mittal, H. Dong, M. Bozkurttas, F. M. Najjar, A. Vargas, and A. von Loebbecke, A versatile sharp interface immersed boundary method for incompressible flows with complex boundaries, J. Comput. Phys. **227**, 4825 (2008).
[38] C. Li, J. Jiang, H. Dong, and K. Zhao, Computational modeling and validation of human nasal airflow under various breathing conditions, J. Biomech. **64**, 59 (2017).
[39] Z. Lou, M. Lei, M. L. Byron, and C. Li, A computational analysis of fluid-structure interaction in metachronal propulsion, in *Proceedings of the ASME 2024 Fluids Engineering Division Summer Meeting collocated with the ASME 2024 Heat Transfer Summer Conference and the ASME 2024 18th International Conference on Energy Sustainability, Anaheim, California*, Computational Fluid Dynamics (CFDTC); Micro and Nano Fluid Dynamics (MNFDTC); Flow Visualization, Vol. 2 (ASME, 2024).
[40] Z. Lou, H.-A. Adrian, M. L. Byron, and C. Li, Hydrodynamics of metachronal motion: effects of spatial asymmetry on the flow interaction between adjacent appendages, in *Proceedings of the ASME 2022 Fluids Engineering Division Summer Meeting, Toronto, Ontario, Canada*, Multiphase Flow (MFTC); Computational Fluid Dynamics (CFDTC); Micro and Nano Fluid Dynamics (MNFDTC), Vol. 2 (ASME, 2022).
[41] M. Lei, Z. Lou, J. Wang, H. Dong, and C. Li, Hydrodynamics of metachronal rowing at intermediate Reynolds numbers, *Proceedings of the ASME 2023 International Mechanical Engineering Congress and Exposition, New Orleans, Louisiana*, Fluids Engineering, Vol. 9 (ASME, 2024).
[42] Z. Lou, M. Lei, H. Dong, C. Li, Z. Lou, M. Lei, H. Dong, and C. Li, Wing–antenna interaction reduces odour fatigue in butterfly odour-tracking flight, J. Fluid Mech. **998**, A45 (2024).
[43] A. T. Bode-Oke and H. Dong, The reverse flight of a monarch butterfly (*Danaus plexippus*) is characterized by a weight-supporting upstroke and postural changes, J. R. Soc. Interface **17**, 20200268 (2020).
[44] C. Li, H. Dong, and B. Cheng, Tip vortices formation and evolution of rotating wings at low Reynolds numbers, Phys. Fluids **32**, 021905 (2020).
[45] G. Liu, H. Dong, and C. Li, Vortex dynamics and new lift enhancement mechanism of wing-body interaction in insect forward flight, J. Fluid Mech. **795**, 634 (2016).
[46] J. Wang, Y. Ren, C. Li, and H. Dong, Computational investigation of wing-body interaction and its lift enhancement effect in hummingbird forward flight, Bioinspir. Biomim. **14**, 046010 (2019).
[47] See Supplemental Material at http://link.aps.org/supplemental/10.1103/PhysRevFluids.10.043103 for the wake structure generated by metachronal motion visualized using Q isosurface.
[48] See Supplemental Material at http://link.aps.org/supplemental/10.1103/PhysRevFluids.10.043103 for the vorticity field of the baseline case from the side view.
[49] See Supplemental Material at http://link.aps.org/supplemental/10.1103/PhysRevFluids.10.043103 for a close-up side view of the tip vortex formation in the baseline case.
[50] See Supplemental Material at http://link.aps.org/supplemental/10.1103/PhysRevFluids.10.043103 for a close-up side view of the tip vortex formation in the P3-only case.

[51] See Supplemental Material at http://link.aps.org/supplemental/10.1103/PhysRevFluids.10.043103 for a close-up bottom view of the edge vortex formation in the baseline case.
[52] See Supplemental Material at http://link.aps.org/supplemental/10.1103/PhysRevFluids.10.043103 for a close-up bottom view of the edge vortex formation in the P3-only case.